

Transparency of Graphene to Solid-Solid van der Waals Interactions

Chuanli Yu¹, Weijia Zeng,¹ Zepu Kou,² Wenxiang Wang,¹ Ling Wang,³ Qunyang Li,³ Xiaofei Liu,² and Zhaohe Dai^{1,*}

¹School of Mechanics and Engineering Science, State Key Laboratory for Turbulence and Complex Systems, Peking University, Beijing 100871, China

²State Key Laboratory of Mechanics and Control for Aerospace Structures, Key Laboratory for Intelligent Nano Materials and Devices of the Ministry of Education, Nanjing University of Aeronautics and Astronautics, Nanjing 210016, China

³AML, Department of Engineering Mechanics, Tsinghua University, Beijing 100084, China



(Received 4 April 2025; accepted 25 August 2025; published 7 October 2025)

Understanding the transparency of two-dimensional (2D) materials to intermolecular interactions—particularly their ability to transmit van der Waals (vdW) forces—is crucial for applications such as the design of 2D material-based nanofluidic and microelectromechanical systems. However, experimental studies have produced inconsistent and even contradictory conclusions regarding the vdW transparency of 2D materials. Here, we employ colloidal atomic force microscopy with a geometrically well-defined probe to measure pull-off and pull-in forces in a model system: graphene on silicon dioxide (SiO_2). Our results reveal that the total vdW force deviates significantly from the naive sum of contributions from graphene and its substrate. Intriguingly, the measured pull-off forces indicate that the effective surface energy of a suspended graphene monolayer can exceed that of its substrate-supported counterpart. Furthermore, our measurements of pull-in forces in substrate-supported systems suggest that graphene of 1–5 layers screens 15%–50% of the intrinsic solid-solid vdW interaction, consistent with Lifshitz theory calculations.

DOI: 10.1103/jgqz-gwlc

It is well established that coating a surface with a single atomic layer—such as a graphene sheet—can dramatically alter its frictional properties and chemical reactivity [1–3]. Recent studies increasingly suggest that graphene coatings also modulate surface energy and adhesion [4–7]. For example, condensation patterns on copper differ markedly between coated and uncoated areas. Furthermore, differences in interfacial energy drive the replacement of the graphene- SiO_2 interface with a graphene-graphene interface on SiO_2 , causing the graphene to peel and tear itself into ribbons spontaneously (dubbed as self-tearing and peeling) [8].

Quantitative experimental measurements of how graphene coatings change the surface energy, however, remain inconclusive [9–12]. Water contact angles (WCAs) can serve as indicators for the effective surface energy of liquid-solid interfaces [13,14] and hence have been extensively used to clarify these effects [4–7]. Yet, the results have been largely inconsistent: graphene coatings have been reported to leave WCAs unchanged, partially altered, or fully modified, which were termed wetting transparency, translucency, or wetting opacity of graphene, respectively [13–18]. Meanwhile, probe-based force measurements are regarded as providing more precise, quantitative insights into graphene-screened solid-solid interactions [19]. However, existing experiments often employ irregularly

shaped probes with uncalibrated and unknown sizes, leading to contradictory conclusions about the extent to which graphene coatings transmit or screen van der Waals (vdW) interactions between solids on two sides of it [20–24].

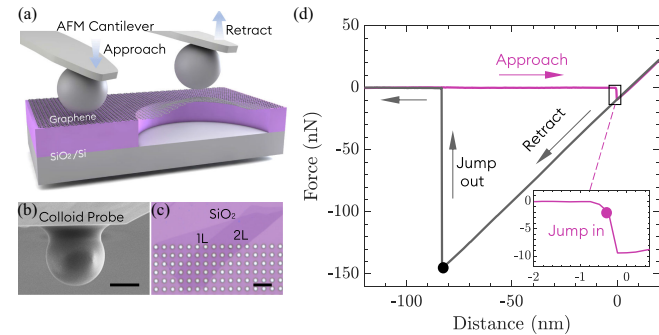


FIG. 1. (a) Schematic illustration of the approach and retraction processes of a spherical AFM probe interacting with supported and suspended graphene. (b) Scanning electron microscopy image of a colloidal SiO_2 probe (radius, $\sim 1 \mu\text{m}$) mounted on an AFM cantilever, used in this study. (c) Optical image of mechanically exfoliated monolayer and bilayer graphene on a SiO_2 substrate patterned with circular cavities to create both supported and suspended regions. (d) Typical AFM force-displacement curve showing pull-in and pull-off instabilities during approach and retraction. Scale bars, 1 μm (b) and 10 μm (c).

*Contact author: daizh@pku.edu.cn

In this Letter, we investigate a simple model system—graphene on a SiO_2 substrate—and systematically quantify its effective surface forces and energies using a spherical colloidal probe with a well-defined geometry [Fig. 1(a)]. By measuring the forces required to approach the probe toward the surface and to separate it under low relative humidity (RH) levels ($< 10\%$), we directly extract the effective (apparent) surface energy and strength of vdW interactions. Our results demonstrate that the overall vdW interaction is far from a simple pairwise addition of contributions from the graphene coating and the underlying substrate because of the complex contact mechanics and many-body effects within the system.

We employ custom-made spherical, SiO_2 colloidal atomic force microscopy (AFM) probes [see the side view in Fig. 1(b) and top view in Supplemental Material, Fig. S2 [25–33]]. This geometry provides a well-defined geometric parameter (sphere radius, R_s), enabling direct conversion of measured forces to surface energies via established contact mechanics models. The most used probes in this Letter feature radii of $\sim 1 \mu\text{m}$ (Fig. S2 [25]). These probes are mounted on AFM cantilevers that function as force sensors during approach and retraction cycles, where the sphere contacts and separates from the surface.

Graphene samples are prepared by mechanically exfoliating graphene onto a SiO_2 substrate prepatterned with circular cavities [Fig. 1(c)]. As such, the graphene is suspended over the cavities and supported by the substrate in other regions. This method avoids the use of chemical-vapor-deposition- (CVD) grown graphene and the organic contamination commonly associated with polymer-assisted transfer techniques [7]. Our experimental setup then enables two key comparisons: (i) between supported and suspended graphene and (ii) between supported graphene sheets with controlled numbers of layers. The comparison between supported and suspended graphene clarifies the vdW transparency of graphene by examining how substrate interactions influence the apparent surface forces of the graphene, whereas the experiments with controlled layer numbers in supported graphene would directly reveal how graphene coatings modify the effective surface properties of the substrate.

Figure 1(d) shows a typical force-displacement curve obtained from AFM-based indentation experiments. During the approach, the microsphere experiences increasing vdW attraction from the surface until it snaps into contact when the sphere-surface gap becomes sufficiently small. We then continue indenting to a predetermined force threshold (approximately 5 nN), after which the sphere is retracted. The critical pull-off force (i.e., the maximum pulling force required to separate the sphere from the surface) is clearly identified at the detachment point, after which the sphere jumps out of contact. Notably, the pull-off force remains largely insensitive to the specific force

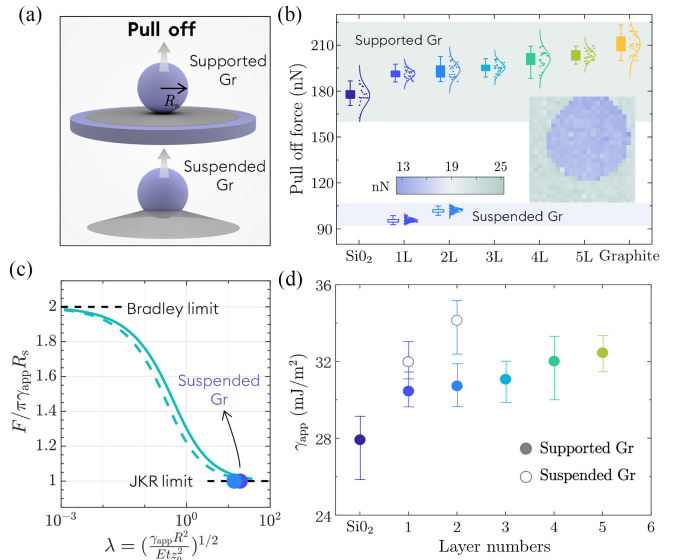


FIG. 2. Pull-off test for vdW transparency of graphene. (a), (b) Schematic and experimental results of pull-off force measurements for substrate-supported and suspended graphene. (b) Inset: a 24×24 array mapping of pull-off forces across a region containing both suspended and supported graphene, with values encoded in the color bar. (c) The transition from the Bradley rigid limit to the JKR limit for clamped, suspended elastic sheets. The solid and dashed curves take $n = 6$, $m = 12$ and $n = 7$, $m = 13$ for Eq. (3) to approximately represent Lennard-Jones potential and retarded vdW interaction, respectively [19]. Experimental data (solid markers) for suspended graphene aligns closely with the JKR limit. (d) The apparent adhesion energy extracted from suspended and supported graphene.

threshold applied (ranging from 3 to 10 nN) in our experiments.

We begin by examining the pull-off measurements, as illustrated in Fig. 2(a). The measured pull-off forces on relatively rigid substrates, including the bare SiO_2 , graphite, and SiO_2 coated with various numbers of graphene layers, are presented in Fig. 2(b). According to the classical contact mechanics models [34], the critical force in these systems, F_{sup} , is directly related to the apparent adhesion energy γ_{app} (i.e., the energy per unit area associated with separating the two solids from their equilibrium contact to an infinite distance [34,35]),

$$\gamma_{\text{app}} = F_{\text{sup}} / (2\pi R_s). \quad (1)$$

This relation, known as the Bradley rigid limit [36], holds remarkably, regardless of the specific interface traction-separation laws, as long as the system is sufficiently rigid [34,37]. Specifically, the validity of Eq. (1) requires a small Tabor parameter, defined as $\mu = (R_s \gamma_{\text{app}}^2 / E_*^2 z_0^3)^{1/3}$, where E_* is the effective Young's modulus of the substrate and z_0 is the equilibrium spacing between the sphere and surface.

Using typical experimental values such as $E_* \gtrsim 70$ GPa, $R_s \sim 1$ μm , $\gamma_{\text{app}} \sim 30$ mJ/m², and $z_0 \sim 0.5$ nm, we have $\mu \lesssim 0.1$, possibly confirming the applicability of the Bradley limit [34,37,38].

For comparison, we also measure the pull-off forces by detaching a sphere from the center of clamped, suspended mono- and bilayer graphene sheets, denoted as F_{sus} [Figs. 2(a) and 2(b)]. Notably, the pull-off force for suspended graphene is systematically smaller—approximately half—compared to that measured for supported graphene. This significant difference can also be observed in the pull-off force mapping with a sharper probe ($R_s \approx 38$ nm for higher spatial resolution) over a region containing both supported and suspended graphene [see the inset of Fig. 2(b)], which clearly outlines the circular suspended area. Interestingly, a similar contrast has been recently observed using ultrasharp AFM tips with radii ($R_s < 10$ nm) [39]. However, this does not necessarily indicate that the adhesion of graphene is systematically lower when being suspended than when being supported. Instead, due to the high flexibility of suspended graphene, the contact mechanics shift into an alternative Johnson-Kendall-Roberts (JKR) regime [40–44], where the apparent adhesion energy is calculated as

$$\gamma_{\text{app}} = F_{\text{sus}} / (\pi R_s). \quad (2)$$

The validity of the JKR limit typically requires a system to be sufficiently compliant. For unstressed thin sheets, this condition has been recently given by $\lambda = (\gamma_{\text{app}} R_s^2 / Et z_0^2)^{1/2} \gg 1$ in Ref. [40], where E and t are Young's modulus and Poisson's ratio of graphene sheets, respectively. To test this condition and, in particular, its universality for various vdW interactions, we combine the membrane elasticity with an interfacial law of the form

$$p_{\text{vdW}}(s) = \frac{(n-4)(m-4)\gamma_{\text{app}}}{(m-n)z_0} \left[\left(\frac{z_0}{s}\right)^{n-3} - \left(\frac{z_0}{s}\right)^{m-3} \right], \quad (3)$$

where n and m are constants, and s is the gap between two surfaces. The form ensures $\gamma_{\text{app}} = \int_{z_0}^{\infty} p_{\text{vdW}} ds$. We find that the pull-off force on suspended graphene follows Eq. (2) for different choices of n and m as long as $\lambda \gg 1$ [Fig. 2(c), see formulation and numerics in Supplemental Material, Note S3 [25]]. In our experiments, $Et \leq 680$ N/m and $\lambda \gtrsim 13$.

Since both the Bradley and JKR limit characterize the vdW adhesion that is independent of the specific form of long-range interactions, we then use Eqs. (1) and (2) to interpret the measured pull-off forces from supported and suspended graphene, respectively [Fig. 2(d)]. For each experimental group, the test was conducted on more than 5 samples, with each sample being measured at least 15 times. As expected, we find that the apparent adhesion of the sphere to the graphene-coated surface (γ_{sgs}) falls between that of the bare SiO₂ substrate (γ_{ss}) and graphite

flakes (γ_{sg}). Note that the layer-dependent trend observed in Fig. 2(d) differs from that reported for graphene peeling from a substrate [45], likely because the characteristic length scale in our setup, given by $\sqrt{z_0 R_s}$, is much greater than the subnanometer surface roughness of the sample, rendering the roughness effects negligible. Unexpectedly, however, comparisons between suspended and supported mono- and bilayer graphene indicate that the effective adhesion energy of the sphere to the suspended graphene sheet (γ_{sg}) can exceed that of its substrate-supported counterpart (γ_{sgs}), suggesting that the substrate may negatively influence the vdW interaction between the sphere and the graphene surface.

Several practical factors may also contribute to this unexpected observation. First, supported and suspended systems might not strictly conform to the ideal Bradley and JKR limits, making the force-to-energy conversion based on Eqs. (1) and (2) not perfectly accurate. Second, in the suspended case, the elastic deformation at the moment of detachment scales as $(\gamma_{\text{app}}/Et)^{1/2} \sim 1\%$, which could lead to a strain-modified surface energy [46,47]. In either scenario, the inherent complexities in contact mechanics seem to preclude a definitive clarification of the apparent adhesion or the vdW transparency of graphene [20–24].

This complexity associated with contact-mode experiments can also be somehow reflected in the observation of the final width w_f of the self-torn graphene ribbon

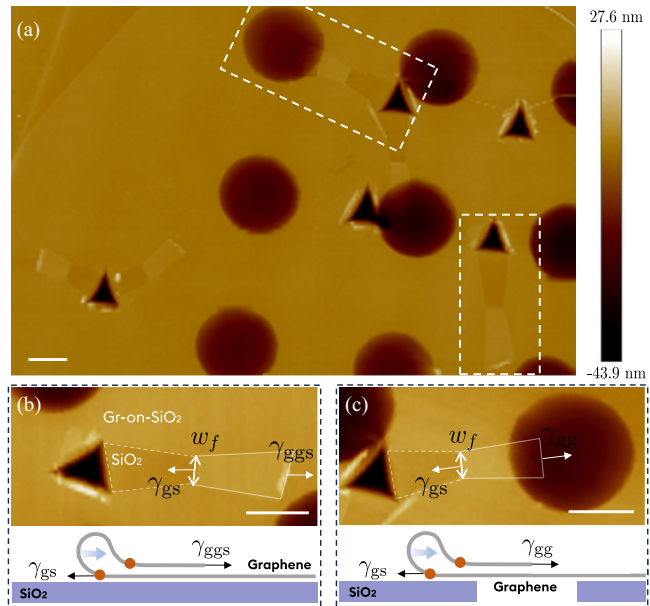


FIG. 3. (a) AFM image of self-peeling behavior in supported and suspended monolayer graphene. (b) AFM image under local magnification and schematic of a self-torn monolayer graphene ribbon on SiO₂ substrate. (c) Self-torn monolayer graphene ribbon with its end resting on suspended graphene. All figures share the same color bar. Scale bars, 1 μm (a), 1 μm (b), and 1 μm (c).

mentioned earlier. In fact, such unusual self-tearing phenomena can be observed not only in various substrate materials [35,48–50], but also in the substrate-free, suspended system, as shown in Fig. 3 (see experimental details in Supplemental Material, Note S1D [25]). Thermodynamically, the ribbons cease to grow when the driving force, defined by the adhesion difference per area $\Delta\gamma$, balances the resistive force provided by the edge fracture energy of the sheet per unit length, $\gamma_{\text{edge}} \approx 5.4 \text{ J nm/m}^2$ [51], leading to a final ribbon width $w_f \sim 2\gamma_{\text{edge}}/\Delta\gamma$ (2 for two cracked edges) [8]. In Fig. 3(b), the adhesion difference $\Delta\gamma$ is given between the adhesion energy of graphene on substrate-supported graphene γ_{ggs} and the adhesion energy of graphene on the bare substrate γ_{gs} , i.e., $\Delta\gamma = \gamma_{\text{ggs}} - \gamma_{\text{gs}}$; w_f is found to range from 323 to 495 nm. In Fig. 3(c), with no substrate present at the end of the ribbon, we have $\Delta\gamma = \gamma_{\text{gg}} - \gamma_{\text{gs}}$, where γ_{gg} is the adhesion of monolayer graphene to suspended graphene; w_f ranges from 400 to 450 nm. Comparing the supported and suspended results suggest that $\gamma_{\text{gg}} - \gamma_{\text{ggs}}$ in the self-tearing system varies from -9.4 to 5.2 mJ/m^2 . The unexpected occurrence of $\gamma_{\text{gg}} > \gamma_{\text{ggs}}$ in the self-peeling and pull-off experiments likely arises from the distinct contact mechanics (and the associated thermal fluctuation states) of graphene in supported versus suspended configurations [52,53].

Therefore, to gain insight into more intrinsic vdW transparency of graphene, we perform contactless pull-in tests [Fig. 4(a)]. For additive vdW interactions, the attractive force between a sphere and a flat surface at a gap D is

$$F_i(D) = \frac{A_i R_s}{6D^2}, \quad (4)$$

where A_i is the Hamaker constant [54], and the subscript i corresponds to sphere-SiO₂ (ss) and sphere-graphite (sg). Note that our focus will be on the pull-in forces for $D \lesssim 15 \text{ nm}$ so that the retardation effect of vdW interactions can be neglected [12,55].

The idea is to first determine A_{ss} and A_{sg} based on tests on SiO₂ and graphite, respectively, and then use these values to interpret the pull-in force F_{tot} measured from an N -layer graphene-coated SiO₂ surface via

$$F_{\text{tot}} = \frac{A_{\text{sg}} R_s}{6D^2} - \frac{A_{\text{sg}} R_s}{6(D + Nt)^2} + \phi(N) \frac{A_{\text{ss}} R_s}{6(D + Nt)^2}, \quad (5)$$

where t is the nominal thickness of graphene and ϕ is the sole fitting parameter characterizing the vdW transparency of the N -layer graphene. Note that such an approach yields direct measurements of A_{ss} , A_{sg} , and $\phi(N)$ all together, in contrast to Refs. [20,24], which employed ultrasharp, irregularly shaped AFM tips with unknown radii.

Figure 4(b) shows a typical F - D dataset measured from thick graphite flakes. Fitting data measured from all samples ($D < 15 \text{ nm}$) with Eq. (4) give $A_{\text{sg}} \approx 1.65 \times 10^{-19} - 1.99 \times 10^{-19} \text{ J}$. Similarly, we observe excellent

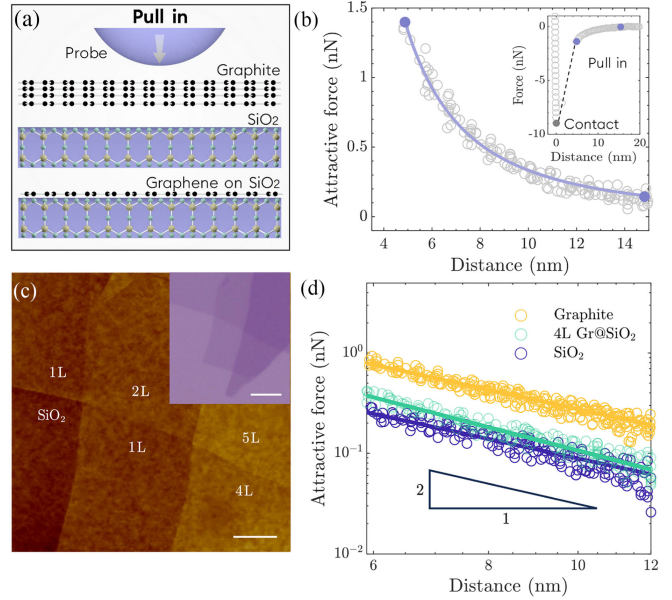


FIG. 4. VdW interactions measured via pull-in tests. (a) Schematic of the pull-in process on graphite, SiO₂, and graphene-coated SiO₂ surfaces. (b) A typical pull-in force data as a function of the gap D between the sphere tip and the graphite surface. The solid curve is a fit to the data for $D < 15 \text{ nm}$ (to avoid the retardation effect), based on Eq. (4). (c) AFM height image of SiO₂-supported graphene of different layer numbers (the inset shows the corresponding optical image of a larger field of view). Scale bars, 2 μm in the main figure and 5 μm in the inset. (d) Comparison of pull-in forces for graphite, four-layer graphene-coated SiO₂, and bare SiO₂.

agreement for bare SiO₂ substrates, obtaining $A_{\text{ss}} \approx 4.96 \times 10^{-20} - 5.69 \times 10^{-20} \text{ J}$ (Supplemental Material, Fig. S4 [25]). These values are comparable to the Hamaker constants reported in the literature, where A_{sg} and A_{ss} range from $1.36 \times 10^{-19} - 2.1 \times 10^{-19} \text{ J}$ [24,56] and $5 \times 10^{-20} - 6 \times 10^{-20} \text{ J}$ [19], respectively.

Using these values, we examine graphene-coated SiO₂ surfaces prepared in the same batch [Fig. 4(c)]. We observe that the corresponding pull-in forces fall between those obtained for graphite and SiO₂. Fitting with the only unknown parameter ϕ yields a good agreement between Eq. (5) and the experimental measurements. The resulting ϕ values range from 50% to 85% and generally decrease with the number of graphene layers [Fig. 5(a)], suggesting 1–5 layer graphene coating would screen 15%–50% of vdW interactions between the two solids on its opposite sides. The reproducibility of our results across different gas atmospheres and controlled humidity levels confirms their robustness within the different applied experimental parameters [see Fig. 5(a) and Supplemental Material, Notes S1 and S2, [25]].

Our findings based on exfoliated graphene, therefore, contrast with previous pull-off tests on CVD-grown graphene (that required direct contact [22]) and pull-in tests on

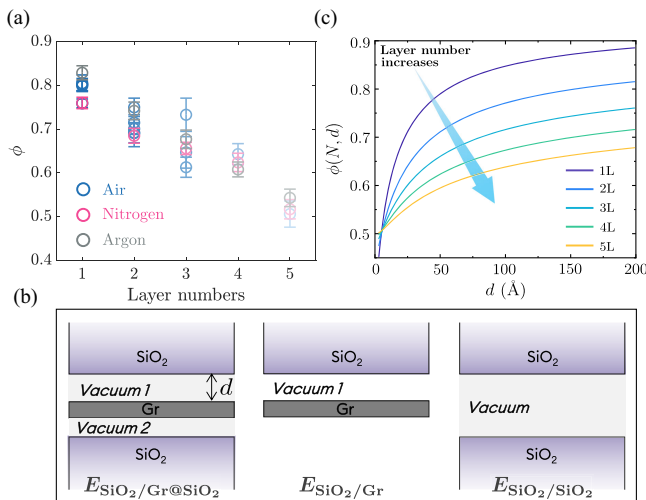


FIG. 5. VdW transparency of graphene obtained through the pull-in experiments and Lifshitz theory calculations. (a) Experimental relationship between the vDW transparency and the number of graphene layers. The RH levels are controlled to be < 10% (air), < 3% (nitrogen), and nearly 0% (argon), respectively (see the setup in Supplemental Material, Note S1E [25]). (b) Schematic illustration of the models used in Lifshitz theory for the calculations. (c) VdW transparency as a function of probe-surface distance and the number of graphene layers, as calculated by Lifshitz theory.

CVD-grown graphene (that employed irregular AFM tips with unknown sizes and did not calibrate the vDW interactions of the bare substrate [20]), both of which suggested an almost complete screening of vDW interactions by graphene (i.e., $\phi \approx 0$). To clarify such discrepancies, we employ the Lifshitz theory to calculate the vDW energy (E) between two surfaces (see details in Supplemental Material, Note S4 in [25]). Lifshitz theory circumvents the additivity approximation by computing interactions directly from bulk dielectric properties [10,11,19]. The probe and substrate were treated as semi-infinite media, while the intermediate graphene was represented as homogeneous continuum layers in the Lifshitz theoretical framework [Fig. 5(b)]. Three configurations are analyzed: $E_{\text{SiO}_2/\text{Gr@SiO}_2}$ (representing probe interacting with graphene-coated SiO₂), $E_{\text{SiO}_2/\text{Gr}}$ (representing probe interacting with merely graphene), and $E_{\text{SiO}_2/\text{SiO}_2}$ (representing probe interacting with the bare SiO₂). The vDW transparency of an N -layer graphene can then be naturally defined by

$$\phi = \frac{E_{\text{SiO}_2/\text{Gr@SiO}_2} - E_{\text{SiO}_2/\text{Gr}}}{E_{\text{SiO}_2/\text{SiO}_2}}, \quad (6)$$

where d denotes the gap between two surfaces.

In Fig. 5(c), we present numerically calculated values of $\phi(N, d)$ as functions of the gap d for various layer numbers of graphene N . The results indicate that the effective vDW

transparency of graphene depends on both its layer number and the probe-surface distance. For a fixed d , ϕ decreases with increasing N , consistent with our experimental observations in Fig. 5(a). Remarkably, despite simplifying the multi-interface electromagnetic reflections into a single ϕ parameter, our experimental results show good agreement with Lifshitz theory calculations for a pull-in distance of around 50 Å [Figs. 5(a) and 5(b)]. Finally, we would like to clarify that the focus of this Letter has been on the measurement of the overall vDW forces based on conventionally processed SiO₂/Si substrates. The presence of hydroxyl groups on the surface may contribute additional Debye (induction) and Keesom (orientation) components to the overall vDW interactions [5,19].

In conclusion, we have demonstrated that graphene coating only partially screens solid-solid vDW interactions. Using standard pull-in experiments with spherical probes, we found that a 1–5 layer graphene coating can screen approximately 15%–50% of the vDW interactions between SiO₂ and SiO₂ when the probe is positioned 5–15 nm above the surface. This result aligns well with Lifshitz theory calculations but contrasts with previous reports suggesting that graphene almost completely screens vDW interactions from the substrate it coats [20]. We should emphasize, however, that in scenarios requiring direct contact with graphene—such as pull-off experiments, WCAs, and peeling—the contact mechanics play a crucial and complex role. Consequently, the apparent energy required for separation from a graphene surface can be found to be comparable and even higher in suspended, flexible configurations than in supported, rigid ones (i.e., the apparent transparency would be zero or even negative), which may explain the conflicting results on ϕ obtained using contact-mode measurements [20–23].

Acknowledgments—This work was supported by the National Natural Science Foundation of China (Grants No. 12372103 and No. 12432003), the National Key Research and Development Program of China (2024YFA1409600), and the Fundamental Research Funds for the Central Universities (NS2024003).

Data availability—The data that support the findings of this Letter are openly available [57].

- [1] T. Fillete, J. L. McChesney, A. Bostwick, E. Rotenberg, K. V. Emtsev, T. Seyller, K. Horn, and R. Bennewitz, *Phys. Rev. Lett.* **102**, 086102 (2009).
- [2] H. Li, C. Tsai, A. L. Koh, L. Cai, A. W. Contryman, A. H. Fragapane, J. Zhao, H. S. Han, H. C. Manoharan, F. Abild-Pedersen *et al.*, *Nat. Mater.* **15**, 48 (2016).
- [3] S. Li, Q. Li, R. W. Carpick, P. Gumbsch, X. Z. Liu, X. Ding, J. Sun, and J. Li, *Nature (London)* **539**, 541 (2016).
- [4] D. Ghoshal, R. Jain, and N. A. Koratkar, *Langmuir* **35**, 12306 (2019).

- [5] P. Snapp, J. M. Kim, C. Cho, J. Leem, M. F. Haque, and S. Nam, *npj Asia Mater.* **12**, 22 (2020).
- [6] C. Yu and Z. Dai, *J. Mater. Inf.* **3**, 20 (2023).
- [7] W. Dong, Z. Dai, L. Liu, and Z. Zhang, *Adv. Mater.* **36**, 2303014 (2024).
- [8] J. Annett and G. L. Cross, *Nature (London)* **535**, 271 (2016).
- [9] J. Hermann, R. A. DiStasio Jr., and A. Tkatchenko, *Chem. Rev.* **117**, 4714 (2017).
- [10] P. Hauseux, A. Ambrosetti, S. P. A. Bordas, and A. Tkatchenko, *Phys. Rev. Lett.* **128**, 106101 (2022).
- [11] X. Liu, Z. Zhang, and W. Guo, *Phys. Rev. B* **97**, 241411(R) (2018).
- [12] M. Li, J. R. Reimers, J. F. Dobson, and T. Gould, *Proc. Natl. Acad. Sci. U.S.A.* **115**, E10295 (2018).
- [13] J. Rafiee, X. Mi, H. Gullapalli, A. V. Thomas, F. Yavari, Y. Shi, P. M. Ajayan, and N. A. Koratkar, *Nat. Mater.* **11**, 217 (2012).
- [14] Z. Li, Y. Wang, A. Kozbial, G. Shenoy, F. Zhou, R. McGinley, P. Ireland, B. Morganstein, A. Kunkel, S. P. Surwade *et al.*, *Nat. Mater.* **12**, 925 (2013).
- [15] C.-J. Shih, Q. H. Wang, S. Lin, K.-C. Park, Z. Jin, M. S. Strano, and D. Blankschtein, *Phys. Rev. Lett.* **109**, 176101 (2012).
- [16] R. Raj, S. C. Maroo, and E. N. Wang, *Nano Lett.* **13**, 1509 (2013).
- [17] C.-J. Shih, M. S. Strano, and D. Blankschtein, *Nat. Mater.* **12**, 866 (2013).
- [18] F. Yang, A. G. Thompson, A. D. McQuain, D. Gundurao, G. Stando, M. A. Kim, H. Liu, and L. Li, *Adv. Mater.* **36**, 2403820 (2024).
- [19] J. N. Israelachvili, *Intermolecular and Surface Forces* (Academic Press, New York, 2011).
- [20] S. Tsoi, P. Dev, A. L. Friedman, R. Stine, J. T. Robinson, T. L. Reinecke, and P. E. Sheehan, *ACS Nano* **8**, 12410 (2014).
- [21] X. Wang, Z. Kou, R. Qiao, Y. Long, B. Li, X. Li, W. Guo, X. Liu, and J. Yin, *Nat. Commun.* **16**, 324 (2025).
- [22] C. D. van Engers, N. E. Cousens, V. Babenko, J. Britton, B. Zappone, N. Grobert, and S. Perkin, *Nano Lett.* **17**, 3815 (2017).
- [23] J. W. Suk, S. R. Na, R. J. Stromberg, D. Stauffer, J. Lee, R. S. Ruoff, and K. M. Liechti, *Carbon* **103**, 63 (2016).
- [24] Y.-C. Chiou, T. A. Olukan, M. A. Almahri, H. Apostoleris, C. H. Chiu, C.-Y. Lai, J.-Y. Lu, S. Santos, I. Almansouri, and M. Chiesa, *Langmuir* **34**, 12335 (2018).
- [25] See Supplemental Material at <http://link.aps.org/supplemental/10.1103/jgqz-gwlc> for details of the experimental method, additional experimental results, and numerical methods, which includes Refs. [26–33].
- [26] J. E. Sader, J. W. Chon, and P. Mulvaney, *Rev. Sci. Instrum.* **70**, 3967 (1999).
- [27] Z. Dai, Y. Hou, D. A. Sanchez, G. Wang, C. J. Brennan, Z. Zhang, L. Liu, and N. Lu, *Phys. Rev. Lett.* **121**, 266101 (2018).
- [28] T. P. Darlington, A. Krayev, V. Venkatesh, R. Saxena, J. W. Kysar, N. J. Borys, D. Jariwala, and P. J. Schuck, *J. Chem. Phys.* **153**, 024702 (2020).
- [29] S. Berciaud, S. Ryu, L. E. Brus, and T. F. Heinz, *Nano Lett.* **9**, 346 (2009).
- [30] T. M. G. Mohiuddin, A. Lombardo, R. R. Nair, A. Bonetti, G. Savini, R. Jalil, N. Bonini, D. M. Basko, C. Galiotis, N. Marzari, K. S. Novoselov, A. K. Geim, and A. C. Ferrari, *Phys. Rev. B* **79**, 205433 (2009).
- [31] Y.-F. Chen, C. M. Kwei, and C. J. Tung, *Phys. Rev. B* **48**, 4373 (1993).
- [32] A. B. Djurišić and E. H. Li, *J. Appl. Phys.* **85**, 7404 (1999).
- [33] V. A. Parsegian, *Van der Waals Forces: A Handbook for Biologists, Chemists, Engineers, and Physicists* (Cambridge University Press, Cambridge, England, 2005).
- [34] J. R. Barber, *Contact Mechanics* (Springer, New York, 2018), Vol. 20.
- [35] Z. Dai, N. Lu, K. M. Liechti, and R. Huang, *Curr. Opin. Solid State Mater. Sci.* **24**, 100837 (2020).
- [36] R. S. Bradley, *Philos. Mag.* **13**, 853 (1932).
- [37] M. Ciavarella, J. Joe, A. Papangelo, and J. Barber, *J. R. Soc. Interface* **16**, 20180738 (2019).
- [38] K. Johnson and J. Greenwood, *J. Colloid Interface Sci.* **192**, 326 (1997).
- [39] S. Zhang, Y. Hou, S. Li, L. Liu, Z. Zhang, X.-Q. Feng, and Q. Li, *Proc. Natl. Acad. Sci. U.S.A.* **116**, 24452 (2019).
- [40] C. Yu, W. Zeng, B. Wang, X. Cui, Z. Gao, J. Yin, L. Liu, X. Wei, Y. Wei, and Z. Dai, *Nano Lett.* **25**, 1876 (2024).
- [41] M. E. Shanahan, *C. R. Acad. Sci. Paris Ser. IV* **1**, 517 (2000).
- [42] F. M. Borodich and B. A. Galanov, *Proc. R. Soc. A* **472**, 20160550 (2016).
- [43] W. Yuan and G. Wang, *Int. J. Solids Struct.* **208**, 214 (2021).
- [44] I. I. Argatov, *Proc. R. Soc. A* **477**, 20210349 (2021).
- [45] S. P. Koenig, N. G. Boddeti, M. L. Dunn, and J. S. Bunch, *Nat. Nanotechnol.* **6**, 543 (2011).
- [46] J. Bico, É. Reyssat, and B. Roman, *Annu. Rev. Fluid Mech.* **50**, 629 (2018).
- [47] R. W. Style, A. Jagota, C.-Y. Hui, and E. R. Dufresne, *Annu. Rev. Condens. Matter Phys.* **8**, 99 (2017).
- [48] D. A. Sanchez, L. Yuan, A. Leventhal, S. Fulco, G. L. Cross, and R. W. Carpick, *Langmuir* **41**, 4491 (2025).
- [49] L. N. Capaldi, L. Yuan, C. Qu, D. A. Sánchez, R. W. Carpick, and O. A. Tertuliano, *Nano Lett.* **25**, 3964 (2025).
- [50] J. C. Rode, D. Zhai, C. Belke, S. J. Hong, H. Schmidt, N. Sandler, and R. J. Haug, *2D Mater.* **6**, 015021 (2018).
- [51] P. Zhang, L. Ma, F. Fan, Z. Zeng, C. Peng, P. E. Loya, Z. Liu, Y. Gong, J. Zhang, X. Zhang *et al.*, *Nat. Commun.* **5**, 1 (2014).
- [52] W. Gao and R. Huang, *J. Mech. Phys. Solids* **66**, 42 (2014).
- [53] F. Ahmadpoor, P. Wang, R. Huang, and P. Sharma, *J. Mech. Phys. Solids* **107**, 294 (2017).
- [54] H. C. Hamaker, *Physica* **4**, 1058 (1937).
- [55] J. N. Israelachvili and D. Tabor, *Proc. R. Soc. A* **331**, 19 (1972).
- [56] B. A. Krajina, L. S. Kocherlakota, and R. M. Overney, *J. Chem. Phys.* **141**, 164707 (2014).
- [57] C. Yu, W. Zeng, Z. Kou, W. Wang, L. Wang, Q. Li, X. Liu, and Z. Dai, 2025, The data that support the findings of this article are openly available at https://github.com/ZhaohDai/2025_PRL.

Supplemental material for
Transparency of graphene to solid-solid van der Waals interactions

Chuanli Yu¹, Weijia Zeng¹, Zepu Kou², Wenxiang Wang¹, Ling Wang³, Qunyang Li³, Xiaofei Liu², Zhaohe Dai^{1,*}

¹*School of Mechanics and Engineering Science, State Key Laboratory for Turbulence and Complex Systems, Peking University, Beijing 100871, China*

²*State Key Laboratory of Mechanics and Control for Aerospace Structures, Key Laboratory for Intelligent Nano Materials and Devices of the Ministry of Education, Nanjing University of Aeronautics and Astronautics, Nanjing 210016, China*

³*AML, Department of Engineering Mechanics, Tsinghua University, Beijing 100084, China*

S1. DETAILED METHODS AND SUPPLEMENTAL EXPERIMENTS

A. Substrate fabrication

Silicon wafers with a 300 nm thermal SiO₂ layer were solvent-cleaned in a laminar-flow hood (RH < 30%) by sequential 5 min sonication in acetone and isopropanol, followed by N₂ blow-dry. Immediately after drying, positive photoresist RH304 (Suzhou Ruihong Electronics, 10 cP) was spun at 500 rpm for 5 s to pre-disperse, then at 3000 rpm for 30 s to yield a 1.2 μm film. The coated wafers underwent a soft bake at 80°C for 20 min to remove residual solvents.

The wafers were transferred to a SÜSS MA/BA6 contact-mode mask aligner, where a photomask defining a square grid of 2 μm diameter circles (5 μm pitch) was aligned and exposed to 365 nm UV light for 5.5 s ($\approx 10 \text{ mW/cm}^2$). Post-exposure development in RH304 developer for 60 s (gentle agitation) revealed the circular resist pattern, which was rinsed with deionized water for 30 s and N₂ dried. A hard bake at 80°C for 20 min was followed to harden the resist, and a brief 30 s O₂ plasma descum (RF 30 W, O₂ pressure 20 mTorr) removed any remaining bottom resist residue.

Etching was performed in an Oxford Instruments PT520 ICP-RIE. The chamber was stabilized at 55 mTorr with SF₆ (4 sccm), CHF₃ (60 sccm), and He (20 sccm) flows, using an ICP power of 300 W and an RF bias of 100 W at a platen temperature of 20 °C. Under these conditions, SiO₂ etching proceeded at 2.5 nm/s; a 120 s etch fully penetrated the 300 nm oxide to expose the silicon substrate, thereby forming clean, vertical-walled holes.

After etching, the wafers were removed and immersed in acetone for 5 min to remove the photoresist, with a brief 10 s ultrasonic assist, followed by a 30 s isopropanol rinse and N₂ blow dry. A final bake at 80°C for 5 min ensured complete removal of organic residues.

B. Preparation of supported and suspended graphene

In AFM tests, supported and suspended graphene flakes with different layer numbers were mechanically exfoliated onto SiO₂/Si pre-patterned substrate described above. These cavities have a depth of approximately 300 nm and a radius of 1.2 μm. In pull-in tests, supported graphene flakes with different layer numbers were mechanically exfoliated onto a silicon wafer with a 300 nm thermal silica layer. Before graphene exfoliation, the SiO₂ substrates were cleaned through sequential ultrasonication in acetone, isopropanol, and deionized water for 5 min each. Following nitrogen drying, oxygen plasma treatment (CIF CPC-F) was conducted for 2 min at 80 W to eliminate surface organic contaminants.

Graphene was mechanically exfoliated from graphite flakes (NGS Naturgraphit GmbH, Germany) using blue adhesive tape (UST, America) in a clean room with relative humidity below 10%. The tape-silica assembly was allowed to rest for 5 minutes before being gently peeled off. To minimize adhesive residue, no heating was applied to the assembly. After exfoliation, the samples were immediately subjected to subsequent testing.

The apparent thickness of the graphene was determined using Raman spectroscopy (Invo-Renishaw system, diode-pumped solid-state laser, 532 nm wavelength). As shown in Fig. S1a, the ratio of the G peak to the 2D peak intensities varies consistently as the number of graphene layers increases from 1 to 4, confirming the layer numbers. Atomic force microscopy (AFM) was employed to check surface condition and supplement the Raman measurements, as shown in Fig. S1b.

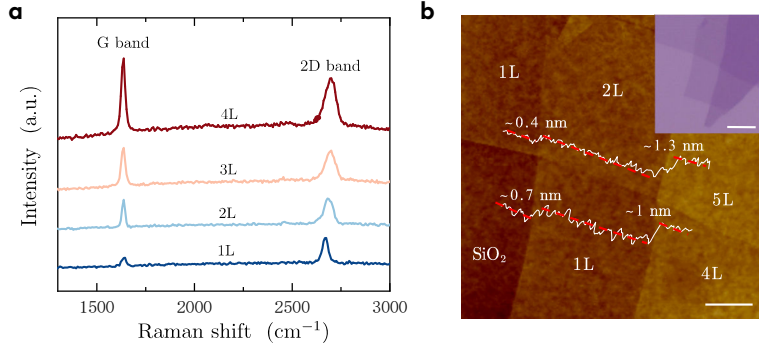


FIG. S1. Characterization of graphene layer number. **a.** Typical Raman spectra of 1-4 layered graphene. **b.** AFM height map and corresponding optical microscope photo of 1-5 layered graphene. Scale bars: 2 μm in AFM map and 5 μm in OM photo.

C. Microspheres and AFM cantilevers

To ensure precise characterization of van der Waals (vdW) interactions, we employed geometrically well-defined spherical probes in our experimental design. In primary investigations, micro-spherical probes with a nominal radius of 1 μm were fabricated by mounting a silicon oxide (SiO_2) microsphere (Tianjin BaseLine ChromTech Research Centre) to a tipless cantilever (Nanosensors TL-FM) using UV-cured adhesive on a micro-nano operation platform. Comparative control experiments utilized probes with radii of approximately 282 nm, which were fabricated by swelling single-crystal silicon (Si) via helium ion dosing performed on triangular pyramid AFM probes (Bruker RTESPA-150). The geometry of probes was measured through scanning electron microscope (SEM) imaging (ZEISS Gemini 300), as shown in Fig. S2. Our measurements were taken after the completion of the whole test for each batch of graphene samples. Only data from probes that did not change significantly in both roughness and radius of curvature (relative to their initially designed state) are used for our analysis.

The stiffness of the cantilever used in the experiments ranges from approximately 1.6 to 2.0 N/m. This range is compliant enough to minimize mechanical damage to the graphene film during scanning while also being sufficiently stiff to ensure a sharp pull-in and pull-off instability during the approach and retraction phases. The stiffness of the cantilever is calibrated using the Sader method [1] whenever the probe is replaced or the AFM header is moved.

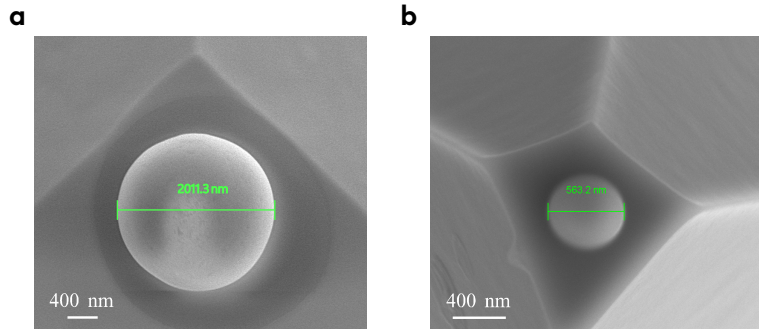


FIG. S2. SEM photos of micro-spherical AFM probes. **a.** Silicon dioxide probe with $2R_s \approx 2011$ nm. **b.** Silicon probe with $2R_s \approx 563.2$ nm.

D. Self-peeling experiments

The self-tearing experiments of graphene (Fig. 3a-c) were performed using a nanoindenter (Bruker Hysitron TI980). Monolayer graphene, mechanically exfoliated onto SiO_2/Si substrates pre-patterned with an array of micro-cavities, with a radius of 1 μm , was subjected to a dot matrix indentation experiment in nanoDMA mode with a frequency of 220 Hz and a target force of 1000 μN . After indentation, the locations of self-tearing were observed using an optical microscope. The surface morphology and characteristic size of the self-torn graphene ribbons were measured using

an AFM (Bruker Multimode 8). We can observe that the graphene ribbons begin to peel away at the edge of the triangular indentation, with their ends supported by substrate-supported or suspended graphene. We then zoom in to scan two representative areas, as shown in Fig. 3b and c in the main text.

The largest sagging observed in the experiment is about 31.9 nm, as shown in Fig. 3a. To assess the effect of sagging on the deformation, we estimate the bending and stretching energy densities. For a sagging depth h , the curvature κ of the suspended graphene with bending stiffness B over the hole of radius R scales as $\kappa \sim h/R^2$. The bending energy density is then estimated as $\mathcal{U}_b \sim B/2\kappa^2 \sim Bh^2/(2R^4) \approx 8 \times 10^{-8} \text{ mJ/m}^2$. The maximum in-plane strain ε at the hole center can be approximated as $\varepsilon \sim 0.74h^2/R^2$ [2]. The associated stretching energy density is $\mathcal{U}_s \sim E_{2D}\varepsilon^2/2 \approx 0.03 \text{ mJ/m}^2$, where E_{2D} is the 2D Young's modulus of graphene. In comparison, the interfacial energy densities involved in the peeling process are approximately 30 mJ/m^2 , which exceed the bending and stretching energy densities by 8 and 3 orders of magnitude, respectively. Thus, the deformation energy due to sagging is negligible relative to the adhesion forces driving the self-peeling behavior.

Numerical calculations of the strain distribution, based on the Föppl–von Kármán equations (following the scheme discussed in [3]), confirm that for a suspended region with $h \approx 30 \text{ nm}$ and $R \approx 1 \mu\text{m}$, the maximum strain remains below 0.1%, agreeing with theoretical estimates, as shown in Fig. S3a and b. Raman G-band mapping on similar suspended regions confirms this. Note that since the substrate effect can also induce the Raman band shift of graphene, we take the Raman G band of 1581 cm^{-1} as a reference point for suspended graphene with zero strain [4]. Using the gauge factor $K = -31 \text{ cm}^{-1}/\%$ [5], the tensile stress in the suspended region is found to be below 0.12%, as shown in Fig. S3d, consistent with the numerical results in Fig. S3b.

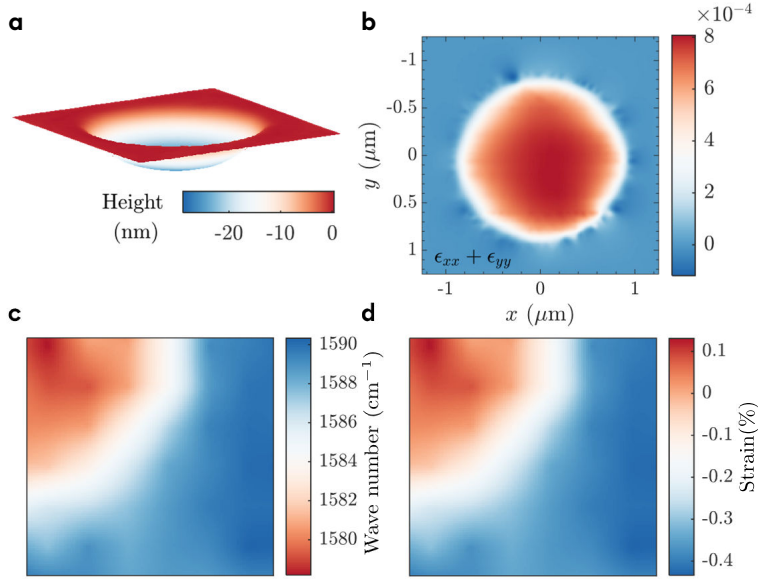


FIG. S3. Strain estimation of graphene in the suspended region. **a,b.** AFM height map and numerically calculated strain of suspended graphene. **c,d.** Raman mapping of G peak positions and strain fields.

E. Pull-off and pull-in experiments

The vdW interaction measurements were conducted using AFM under three gas environments. For suspended graphene, the measurement procedure began with an initial scan to determine the radius of the suspended region and precisely locate its center. The AFM cantilever was then driven downward at a speed of 400 nm/s , ensuring that the spherical probe contacted the center of the graphene film. After reaching the target indentation force of 20 nN , the probe was retracted at the same speed. Force-displacement curves were recorded at each test point, with tests repeated at least 10 times to ensure reliability. For supported graphene, measurements were performed in air (Bruker Multimode 8, RH < 10%), and nitrogen (Bruker Multimode 8 equipped with a custom-built environmental chamber, RH < 3%), argon (Bruker Dimension Icon housed in a glove box, water content < 0.01 ppm). At each condition, measurements were repeated three times at a single location, and at least five distinct locations were tested for each thickness.

Array indentation tests for the inset in Fig. 3b of the main text were performed under the same parameters

with a spacing of 120 nm. In this case, we used a spherical probe with $R_s \approx 38$ nm. A MATLAB toolbox (e.g., *BrukerAFMToolBox*) was used for batch processing, including baseline correction and force-displacement data extraction.

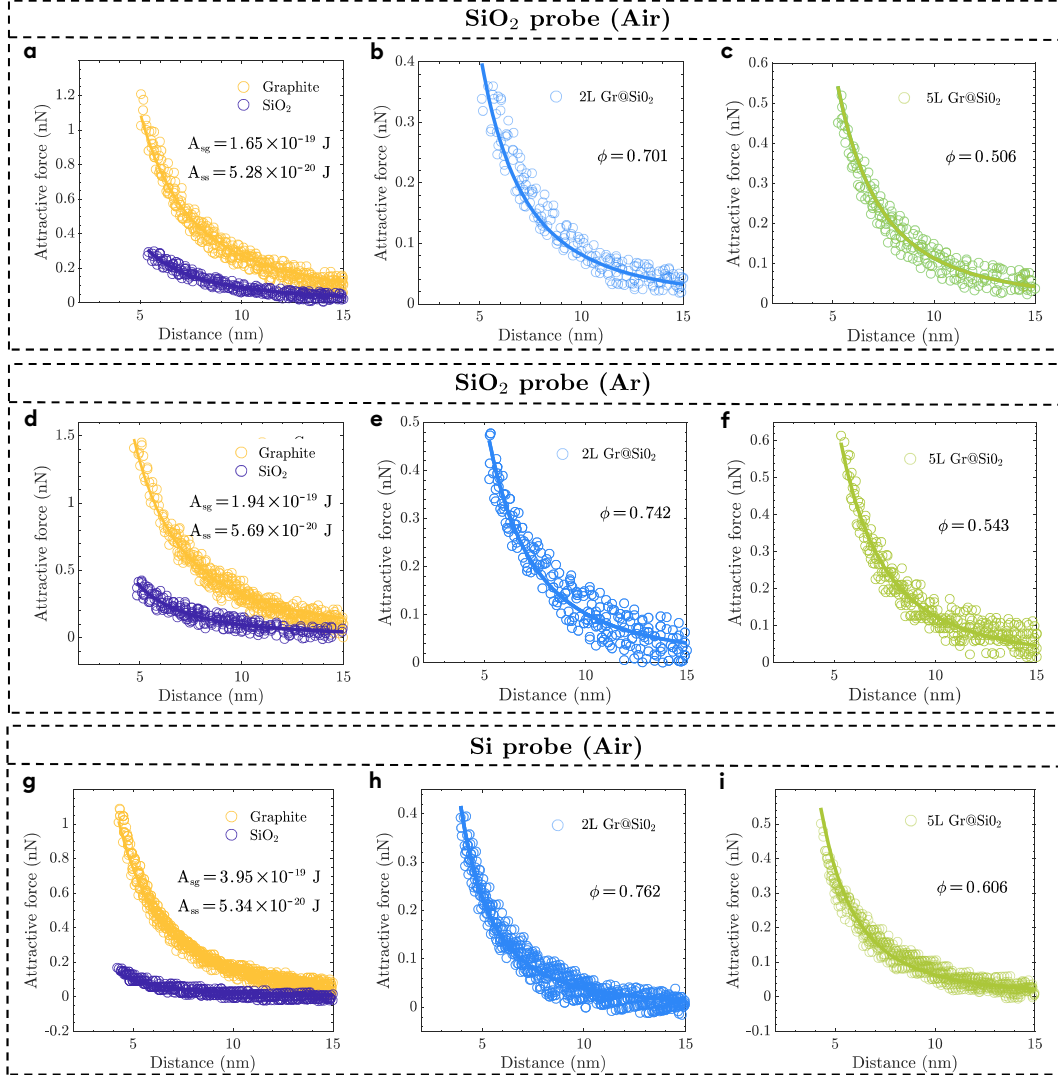


FIG. S4. Force-displacement curves recorded in pull-in results and their fitting curves. a,d,g. Graphite and Bare SiO₂ substrate; **b,e,h.** Bilayer graphene-coated SiO₂ substrate; **c,f,i.** 5L graphene-coated SiO₂ substrate; Note that (a-c) used SiO₂ probes under air, (d-f) used SiO₂ probes under argon, and (g-i) used Si probes under air.

Fig. S4 presents the processing of the experimental data obtained using SiO₂ and Si tips in air and argon atmospheres. Curves from the same dataset are superimposed, and the corresponding Hamaker constants, A_{ss} and A_{sg} , are determined by fitting to Eq. (4) in the main text, as shown in Fig. S4a and d. These fitted Hamaker constants are then substituted as known values into Eq. (5) in the main text to determine the vdW transparency, ϕ , for different numbers of graphene layers. As illustrated in Fig. S4, for the SiO₂ tip, the data obtained in air and argon under controlled humidity showed good fits and similar Hamaker constants. We also note that the values measured with the Si tip may deviate slightly from the theoretical predictions due to the unavoidable 1–2 nm oxide layer on the surface, although a good fit is still obtained.

We investigated the influence of approach speeds on the pull-in behavior of the supported bilayer graphene. The approach speed is set in the range of 100–1000 nm/s, and the corresponding force-displacement curves are shown in Fig. S5. It can be observed that speed does not significantly influence the pull-in process and has almost no effect on the critical distance or critical force required for the pull-in process within the speed range. Therefore, it can be concluded that the speed range we applied has a minimal impact on these dynamics. In summary, the approach speed of 400 nm/s used in the experiment can be considered representative of typical conditions.

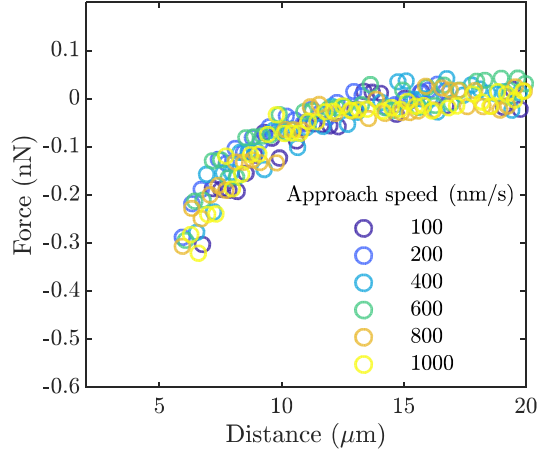


FIG. S5. The negligible dependency of pull-in behavior on the approach speed. All data in this work were obtained at an approach velocity of 400 nm/s.

S2. PITFALLS AND PRECAUTIONS

A. Hydrocarbon and adhesive contamination

Potential contamination, such as adhesive residues or air hydrocarbons on or trapped between graphene and SiO_2 may artificially modulate the vdW interactions. In the following, we discuss the processes for successful and unsuccessful fabrications and characterizations.

The $500\ \mu\text{m}$ thick substrates, consisting of an undoped, amorphous 300 nm thermal SiO_2 layer on N-type-doped Si ($\rho < 0.005\ \Omega\cdot\text{cm}$) from PrMat company, were stored in high-vacuum chambers ($< 10^{-6}\ \text{mbar}$). Pre-plasma treatment (80 W, 2 min) is very effective in removing surface organic contaminations. Graphene was mechanically exfoliated on pre-patterned substrates using a UST blue adhesive tape in the cleanroom. The process yielded three distinct regions (Fig. S6a and b): (i) Graphene regions: Freshly dissociated graphene flakes (1-5L) without tape contact (darker patches); (ii) Clean SiO_2 regions: No graphene adsorbed, but the tape did not touch the SiO_2 substrate (outlined by the white dashed line); (iii) Contaminated regions: Tape-contacted areas (outside the gray dashed line, traces of adhesive contamination are obvious). Obviously, successful experiments need to focus on clean regions.

In experiments, there is a straightforward way to judge whether the area is contaminated. First, contact-mode AFM scans (Bruker RTESPA-300 probe, spring constant $k = 23\ \text{N/m}$, setpoint 150 nN) of $5 \times 5\ \mu\text{m}^2$ SiO_2 (orange frame) and graphene (green frame) regions, alongside a larger $10 \times 10\ \mu\text{m}^2$ tapping-mode scan. Surfaces can be considered clean if no ridges are observed around the scanned areas, as shown in Fig. S6c. A more accurate way to test the interface cleanliness can be given by TEM imaging. Cross sections were obtained using a focused ion beam (FIB, Nova200 NanoLab), followed by TEM (Thermo Scientific Spectra 300) imaging, which confirmed pristine graphene/ SiO_2 interfaces with clean morphology and spacing $< 5\ \text{\AA}$ (Fig. S7).

B. Humidity Dependency

Ambient water layers could introduce capillary forces that interfere with the measurement of vdW interactions. Our humidity management strategy included:

All experiments were conducted in a humidity-stabilized cleanroom with a desiccant dehumidifier. Experiments conducted under three environmental conditions reveal the low humidity sensitivity under applied controlled conditions, as shown in Fig. 5a and S4.

To further confirm, the pull-off and pull-in tests were performed between SiO_2 microsphere ($R_s \approx 1\ \mu\text{m}$) and SiO_2 substrate at various relative humidities (RH=1.8%, 5%, 10%, 15%, and 65%), as shown in Fig. S8. The approach force-distance curves and pull-off forces remained consistent across these conditions. The fitted Hamaker constants are in the range of $4.96 - 5.95 \times 10^{-20}\ \text{J}$, which is very close to the previously reported experimental values ($5 - 6 \times 10^{-20}\ \text{J}$) [6], indicating that our measurements are largely insensitive to low humidity levels. As shown in Fig. S8b, at higher RH (e.g., 65%), water menisci can form between the AFM tip and the sample, leading to jump-in events at much larger separations (on the order of 100 nm), which makes accurate measurement of vdW forces impossible.

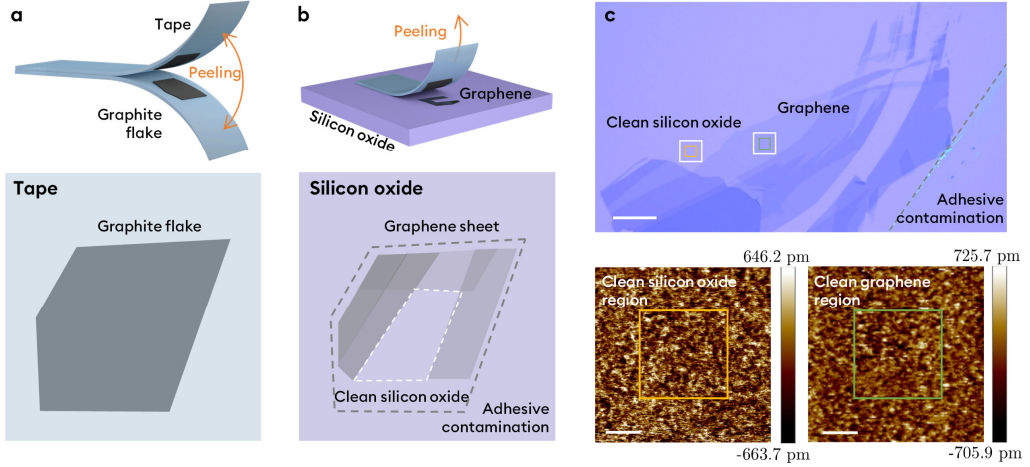


FIG. S6. Mechanical exfoliation process and interface validation. **a.** Schematic of graphite dissociation during tape exfoliation; **b.** Resultant graphene adhesion on SiO_2 substrate.; **c.** Optical microscopy and AFM verification of contaminant-free surfaces.

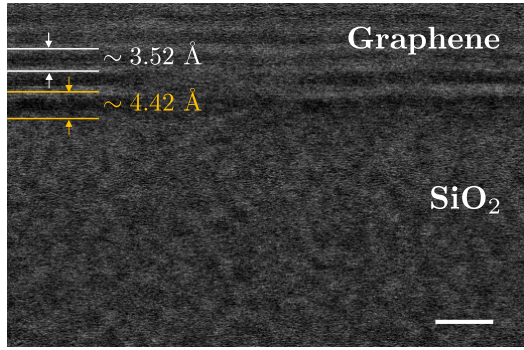


FIG. S7. TEM image of the longitudinal section of graphene on SiO_2 shows no contamination at the interface and the interfacial spacing is less than 5 Å. Scale bar: 1 nm.

C. Hydroxyl Groups and Electrostatic Forces

Hydroxyl (-OH) groups on SiO_2 and the lower silicon doping could introduce interference effects. The declarations are as follows:

The silica substrate used in our experiments is amorphous and may contain a small number of isolated surface OH groups. These hydroxyl groups could contribute additional Debye (induction) and Keesom (orientation) components to the overall van der Waals (vdW) interactions, making their contribution slightly more significant relative to the London dispersion forces. However, based on the absence of observable adsorbed water layers in our TEM characterization, we anticipate only a limited presence of OH groups. For this reason, rather than attempting to quantitatively separate the individual contributions of Debye, Keesom, and dispersion forces, the focus of this is on measuring the apparent vdW transparency of conventionally processed SiO_2/Si substrates, as this approach is more broadly relevant for guiding routine vdW interaction measurements and micro/nano-device fabrication.

The silicon substrate beneath the SiO_2 layer is heavily N-type doped with a resistivity $\rho < 0.005 \Omega \cdot \text{cm}$, yielding a carrier concentration calculated as $n = 1/(e\mu_n\rho) \approx 1.04 \times 10^{19} \text{ cm}^{-3}$, where e is the electron charge and μ_n is the electron mobility (Here $\mu_n = 120 \text{ cm}^2/\text{V} \cdot \text{s}$ for highly doped silicon). The resulting Debye screening length is $\lambda_D = \sqrt{\varepsilon_r\varepsilon_0 k_B T / (e^2 n)} \approx 1.27 \text{ nm}$, where ε_r is silicon's relative permittivity, ε_0 is the vacuum permittivity, k_B is Boltzmann's constant, and T is temperature. This screening length, significantly smaller than the SiO_2 thickness of 300 nm, ensures that electrostatic interactions from substrate doping are effectively screened and do not affect van der Waals interaction measurements.

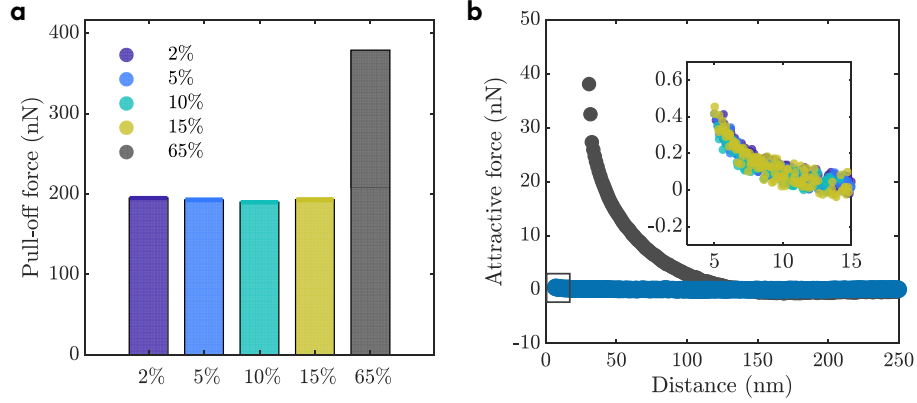


FIG. S8. Humidity-dependent van der Waals interactions between a sphere and a SiO_2 surface. **a.** Pull-off forces at relative humidity (RH) levels of 2%, 5%, 10%, 15%, and 65%. **b.** Representative force-distance curves during approach at the same RH levels.

S3. MODELING MEMBRANE DEFORMATION AND VAN DER WAALS INTERACTION

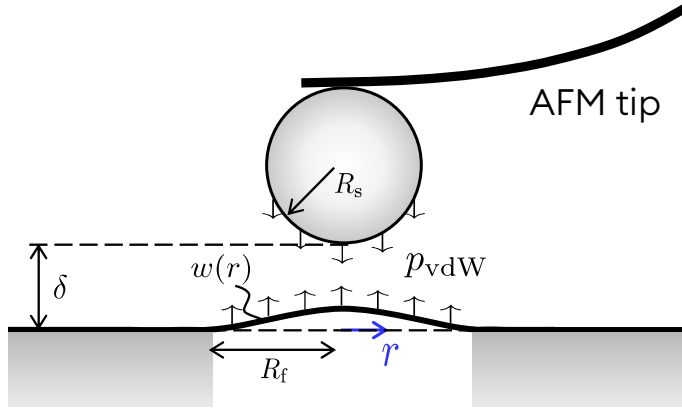


FIG. S9. Schematic of the indentation of a clamped, suspended graphene sheet. We use Derjaguin approximation so that sphere shape is approximated by a paraboloid and the sphere-graphene gap is given by $s(r) = \delta + r^2/(2R_s) - w(r)$, where δ is the vertical position of the sphere tip, R_s is the sphere radius, $w(r)$ is the deformed profile of the sheet under vdw attraction from the sphere.

We established a self-consistent model to bridge the JKR and Bradley limits. In this model, we assume that the slope of the deformed membrane is moderate, thus, it is appropriate to take the Föppl–von Kármán equation as the vertical equilibrium equation. Since the bending effect for single and bilayer graphene is small and ignored for simplicity, the governing equation for the deflection of the film $w(r)$ then reads

$$\frac{1}{r} \frac{d\varphi}{dr} \frac{dw}{dr} + \frac{\varphi}{r} \frac{d^2w}{dr^2} + p_{\text{vdW}}(s) = 0, \quad (\text{S.1})$$

where $s \approx \delta + \frac{r^2}{2R_s} - w(r)$ (see Fig. S9), d is the gap between the surfaces of sphere and the membrane, δ is the height of the sphere tip, p_{vdW} is the vdw force per unit area between the sphere and the surface given in Eq. (3) in the main text. We will focus on the Lennard-Jones type potential with $n = 6$ and $m = 12$ given in Eq. (3) in the main text, and φ is the stress function linking the radial and hoop stress resultants via

$$N_{rr} = \frac{\varphi}{r} \quad \text{and} \quad N_{\theta\theta} = \frac{d\varphi}{dr}, \quad (\text{S.2})$$

respectively. This treatment makes the equilibrium equations in the horizontal direction hold automatically. Furthermore, we need another equation, i.e., the geometric compatibility equation to describe the deformation behavior of

the film completely:

$$\frac{d\varphi}{dr} - \frac{\varphi}{r} + r \frac{d^2\varphi}{dr^2} + \frac{1}{2} Et \left(\frac{dw}{dr} \right)^2 = 0. \quad (\text{S.3})$$

Utilizing axisymmetric properties of the system, we obtain the boundary conditions at the membrane center:

$$w'(0) = 0, \quad u(0) = \lim_{r \rightarrow 0} \frac{r\varphi'(r) - \nu\varphi(r)}{Et} = 0, \quad (\text{S.4})$$

and the boundary conditions at the edge of the membrane are also easy to give

$$w(R_f) = 0, \quad \varepsilon_\theta(R_f) = \frac{u(R_f)}{R_f} = \frac{\varphi'(R_f) - \nu\varphi(R_f)/R_f}{Et} = \frac{(1-\nu)T_{\text{pre}}}{Et}, \quad (\text{S.5})$$

where T_{pre} is the residual stress that can be neglected (as no pressure is applied to the film) and R_f is the radius of the membrane. Besides, since the length scale z_0 comes into play, we find the sole, corresponding controlling parameter after non-dimensionalization is given by

$$\lambda = \left(\frac{\gamma_{\text{app}} R_s^2}{Et z_0^2} \right)^{1/2}. \quad (\text{S.6})$$

Specifically, we take the equilibrium distance z_0 as the vertical characteristic length and $\sqrt{R_s z_0}$ as the horizontal characteristic length. Therefore, we introduce the normalized physic quantities as

$$W = \frac{w}{z_0}, \quad \Phi = \frac{\varphi R_s^{1/2}}{Et z_0^{3/2}}, \quad \rho = \frac{r}{(R_s z_0)^{1/2}}, \quad \mathcal{R}_f = \frac{R_f}{(R_s z_0)^{1/2}}, \quad \mathcal{R}_s = \frac{R_s}{(R_s z_0)^{1/2}}, \quad \Delta = \frac{\delta}{z_0}, \quad S = \frac{s}{z_0}. \quad (\text{S.7})$$

Taking the vdW pressure with $n = 6$ and $m = 12$ in Eq. (3) in the main text, we can obtain the nondimensionalized governing equations as

$$\frac{\Phi}{\rho} \frac{d^2 W}{d\rho^2} + \frac{1}{\rho} \frac{d\Phi}{d\rho} \frac{dW}{d\rho} + \frac{8}{3} \lambda^2 \left(\frac{1}{S^3} - \frac{1}{S^9} \right) = 0, \quad (\text{S.8})$$

where $S(\rho) \approx \Delta + \frac{\rho^2}{2} - W(\rho)$ and

$$\frac{d\Phi}{d\rho} - \frac{\Phi}{\rho} + \rho \frac{d^2\Phi}{d\rho^2} + \frac{1}{2} \left(\frac{dW}{d\rho} \right)^2 = 0. \quad (\text{S.9})$$

The boundary conditions are

$$\begin{cases} W'(0) = 0, \lim_{\rho \rightarrow 0} (\rho\Phi'(\rho) - \nu\Phi(\rho)) = 0, \\ W(\mathcal{R}_f) = 0, \Phi'(\mathcal{R}_f) - \nu \frac{\Phi(\mathcal{R}_f)}{\mathcal{R}_f} = 0. \end{cases} \quad (\text{S.10})$$

Therefore, under prescribed indentation depth Δ and sheet radius \mathcal{R}_f , this system is *only controlled by the “transition parameter”* λ , defined in Eq. (S.6). This is also true by taking $n = 7$ and $m = 13$ or other combinations ($n > 4, m > n + 2$) for the vdW pressure in Eq. (3) in the main text. We discretize this highly nonlinear boundary value problem using central finite differences and obtain a set of algebraic equations, which are solved using successive over-relaxation of the Newton method.

S4. CALCULATION OF VAN DER WAALS TRANSPARENCY USING LIFSHITZ THEORY

In this section, we calculate the vdW transparency in the graphene@SiO₂ system using Lifshitz theory. Two probe materials—SiO₂ and Si—are considered. Here, we present the derivation for the SiO₂ case, noting that the derivation for Si follows a similar procedure. As illustrated in Fig. S10, both the SiO₂ probe and the SiO₂ substrate are modeled as semi-infinite media. Graphene, comprising varying numbers of layers, is approximated as a continuous plate, with each layer assigned a thickness of 3.4 Å. The separation between the bottom surface of the graphene plate and the

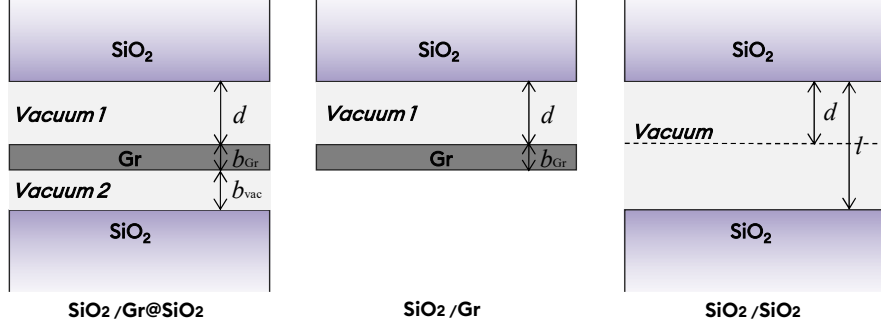


FIG. S10. Illustration of models used in the Lifshitz theory for the calculation of the vdW attenuation function.
a. Model used to calculate the vdW energy between semi-infinite SiO_2 and graphene supported by a semi-infinite SiO_2 substrate.
b. Model used to calculate the vdW energy between SiO_2 and suspended graphene. **c.** Model used to calculate the vdW energy between SiO_2 and the SiO_2 substrate.

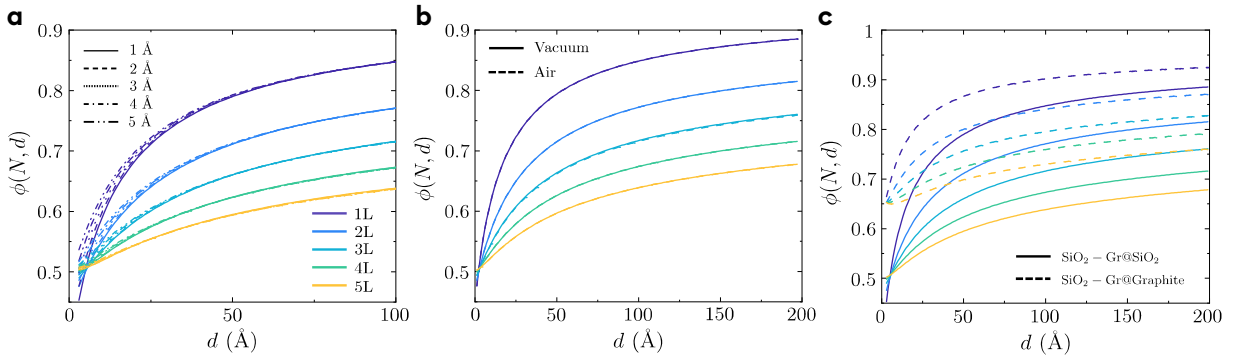


FIG. S11. The vdW attenuation coefficient as a function of graphene layers N and the gap d between the probe and the material. **a.** Effect of different vdW equilibrium distances on vdW attenuation function. **b.** Effect of different intermediate media across the graphene- SiO_2 interface. **C.** Effect of different substrates on vdW attenuation function ($b_{\text{vac}} = 1 \text{ \AA}$).

SiO_2 substrate, denoted as b_{vac} , is does not include the thickness of graphene (so the true height of the graphene is $b_{\text{vac}} + 3.4 \text{ \AA}$). The dielectric functions of the materials are adopted from previous studies [7, 8].

The vdW energy between a semi-infinite SiO_2 and SiO_2 supported graphene is given by [9]

$$E_{\text{SiO}_2/\text{Gr@SiO}_2} = \frac{k_B T}{8\pi d^2} \sum_{n=0}^{\infty}' \int_{r_n}^{\infty} x \ln \left(1 - \bar{\Delta}_{\text{SiO}_2/\text{vac}1} \bar{\Delta}_{\text{Gr}/\text{vac}1}^{\text{eff}} e^{-x} \right) dx, \quad (\text{S.11})$$

where k_B and T are the Boltzmann constant and temperature, respectively. The variable x in the integrand represents the modulus of the in-plane wave vector, and the starting point of integration r_n is defined as $r_n = 2l\varepsilon_m^{1/2}\xi_n$, where the Matsubara frequency ξ_n is defined as $\xi_n = 2\pi k_B T n / \hbar$, and \hbar is the reduced Planck's constant. The prime symbol on the summation sign indicates that the zero-frequency term is multiplied by 1/2. The Fresnel reflection coefficient at the interface between SiO_2 and vacuum is given by:

$$\bar{\Delta}_{\text{SiO}_2/\text{vac}1} = \frac{x\varepsilon_{\text{SiO}_2} - x_{\text{SiO}_2}\varepsilon_{\text{vac}}}{x\varepsilon_{\text{SiO}_2} + x_{\text{SiO}_2}\varepsilon_{\text{vac}}}, \quad (\text{S.12})$$

where $x_{\text{SiO}_2}^2 = x^2 + (2d\xi_n/c)^2(\varepsilon_{\text{SiO}_2} - \varepsilon_{\text{vac}})$ and ε is the dielectric constant. The effective Fresnel coefficient at the interface between graphene and vacuum $\bar{\Delta}_{\text{Gr}/\text{vac}1}^{\text{eff}}$ is found in [9]. The two-body SiO_2 /graphene and SiO_2 / SiO_2 vdW energies ($E_{\text{SiO}_2/\text{Gr}}$ and $E_{\text{SiO}_2/\text{SiO}_2}$) were calculated for the corresponding bilayer without the presence of a third layer. To provide insight into the many-body effect, the vdW attenuation function is defined as:

$$\phi(N, d) = \frac{E_{\text{SiO}_2/\text{Gr@SiO}_2} - E_{\text{SiO}_2/\text{Gr}}}{E_{\text{SiO}_2/\text{SiO}_2}}. \quad (\text{S.13})$$

We analyze the vdW transparency as a function of the number of graphene layers N and the gap d between the probe and the material, as illustrated in Fig. S11. Due to the lack of consensus regarding the vdW equilibrium distance between graphene and the SiO_2 substrate, we calculated different cases with $b_{\text{vac}} = 1 \text{ \AA}$ to 5 \AA , respectively. Fig. S11a demonstrates that ϕ exhibits minimal dependence on b_{vac} . Additionally, we investigated the effects of different intermediate media between graphene and SiO_2 . The Fig. S11b shows similar results in air and vacuum due to their nearly identical dielectric constants. We finally consider the vdW decay in the $\text{SiO}_2/\text{graphene}@\text{graphite}$ system. As shown in Fig. S11c, compared with the SiO_2 substrate, the vdW transparency between graphite's homogeneous layers is significantly weaker. This result indicates that the error introduced by neglecting the vdW decay between graphene layers (i.e., assuming complete linear superposition) in the main text is negligible.

- [1] John E Sader, James WM Chon, and Paul Mulvaney, “Calibration of rectangular atomic force microscope cantilevers,” *Rev. Sci. Instrum.* **70**, 3967–3969 (1999).
- [2] Zhaohe Dai, Yuan Hou, Daniel A. Sanchez, Guorui Wang, Christopher J. Brennan, Zhong Zhang, Luqi Liu, and Nanshu Lu, “Interface-governed deformation of nanobubbles and nanotents formed by two-dimensional materials,” *Phys. Rev. Lett.* **121**, 266101 (2018).
- [3] Thomas P Darlington, Andrey Krayev, Vishal Venkatesh, Ravindra Saxena, Jeffrey W Kysar, Nicholas J Borys, Deep Jariwala, and P James Schuck, “Facile and quantitative estimation of strain in nanobubbles with arbitrary symmetry in 2d semiconductors verified using hyperspectral nano-optical imaging,” *J. Chem. Phys.* **153** (2020).
- [4] Stéphane Berciaud, Sunmin Ryu, Louis E Brus, and Tony F Heinz, “Probing the intrinsic properties of exfoliated graphene: Raman spectroscopy of free-standing monolayers,” *Nano Lett.* **9**, 346–352 (2009).
- [5] TMG Mohiuddin, Antonio Lombardo, RR Nair, A Bonetti, G Savini, R Jalil, Nicola Bonini, DM Basko, C Gallois, Nicola Marzari, *et al.*, “Uniaxial strain in graphene by raman spectroscopy: G peak splitting, grüneisen parameters, and sample orientation,” *Phys. Rev. B* **79**, 205433 (2009).
- [6] Jacob N Israelachvili, *Intermolecular and surface forces* (Academic Press, 2011).
- [7] Yung-Fu Chen, CM Kwei, and CJ Tung, “Optical-constants model for semiconductors and insulators,” *Phys. Rev. B* **48**, 4373 (1993).
- [8] Aleksandra B Djurišić and E Herbert Li, “Optical properties of graphite,” *J. Appl. Phys.* **85**, 7404–7410 (1999).
- [9] V Adrian Parsegian, *Van der Waals forces: a handbook for biologists, chemists, engineers, and physicists* (Cambridge University Press, 2005).